

Article

Pedestrian-Level Urban Wind Flow Enhancement with Wind Catchers

Lup Wai Chew ^{1,*}, Negin Nazarian ² and Leslie Norford ³

¹ Department of Mechanical Engineering, Massachusetts Institute of Technology, Cambridge, MA 02139, USA

² Center for Environmental Sensing and Modeling, Singapore-MIT Alliance for Research and Technology, Singapore 138602, Singapore; negin@smart.mit.edu

³ Department of Architecture, Massachusetts Institute of Technology, Cambridge, MA 02139, USA; lnorford@mit.edu

* Correspondence: lupwai@mit.edu

Received: 10 July 2017; Accepted: 22 August 2017; Published: 25 August 2017

Abstract: Dense urban areas restrict air movement, causing airflow in urban street canyons to be much lower than the flow above buildings. Boosting near-ground wind speed can enhance thermal comfort in warm climates by increasing skin convective heat transfer. We explored the potential of a wind catcher to direct atmospheric wind into urban street canyons. We arranged scaled-down models of buildings with a wind catcher prototype in a water channel to simulate flow across two-dimensional urban street canyons. Velocity profiles were measured with Acoustic Doppler Velocimeters. Experiments showed that a wind catcher enhances pedestrian-level wind speed in the target canyon by 2.5 times. The flow enhancement is local to the target canyon with little effect in other canyons. With reversed flow direction, a “reversed wind catcher” has no effect in the target canyon but reduces the flow in the immediate downstream canyon. The reversed wind catcher exhibits a similar blockage effect of a tall building amid an array of lower buildings. Next, we validated Computational Fluid Dynamics (CFD) simulations of all cases with experiments and extended the study to reveal impacts on three-dimensional ensembles of buildings. A wind catcher with closed sidewalls enhances maximum pedestrian-level wind speed in three-dimensional canyons by four times. Our results encourage better designs of wind catchers to increase wind speed in targeted areas.

Keywords: urban street canyon; wind enhancement; architectural intervention; water channel experiment; CFD simulation; passive ventilation

1. Introduction

In the process of urbanization, natural land covers are replaced with built materials and, consequently, the land surface roughness is significantly modified [1]. These alterations further impact the airflow in urban areas, as tall buildings obstruct and separate the wind [2–4] and canyon vortices are formed in urban street canyons [5–7], often resulting in a low wind speed near the ground or at the pedestrian level.

The importance of pedestrian-level ventilation in an urban environment is manifold. First, urban areas are severely subjected to the urban heat island (UHI) phenomena [8–12], which is in part due to the decreased momentum and heat exchange from the land surface to the atmosphere in the street canyons [13]. Subsequently, poor pedestrian-level ventilation can exacerbate UHI [5,13] and exposes urban dwellers to a higher air temperature. This factor, together with the decreased wind speed at the pedestrian level, cause a significant threat to human thermal comfort in urban areas [14]. Second, building energy consumption is closely tied with the pedestrian-level ventilation and the canyon air temperature [15]. Accordingly, improving ventilation in street canyons is instrumental for achieving a low-energy urban design [16]. Lastly, with the increased rate of emissions in urban

areas, air quality in street canyons and city breathability for urban dwellers are closely tied to the efficiency of the city to ventilate itself [17–21]. Therefore, it is paramount that we evaluate the methods of enhancing wind speed in urban street canyons.

The role of urban morphology and architectural elements on urban flow and thermal field is indisputable. For instance, canyon aspect (height-to-width) ratio has been identified as one of the most important parameters in categorizing the flow field inside an urban street canyon [5–7]. Additionally, the drag coefficient and flow field in the urban canopy layer are strongly dominated by the urban packing density [18,22,23] and the layout of building arrays [24,25]. These studies also demonstrated that the geometrical inhomogeneity in urban design (e.g., building configurations and variability of street width) significantly modifies the local ventilation capacity, and Hang et al. [7] showed that height variability determines the momentum flux as well as the removal of pedestrian-level pollutants in urban street canyons.

In addition to the street-to-meso scale features of urban morphology, small-scale features of the street architecture also influence urban airflow [26]. Several studies provided evidence that roof shapes significantly modify the urban airflow and dispersion [27,28]. Huang et al. [29] demonstrated that different orientations of wedge-shaped roofs significantly alter the structure of circulation vortices induced in the canyons. Abohela et al. [30] evaluated the effects of roof shape on above-roof flow acceleration and found that a vaulted roof produces the largest flow acceleration in an aligned wind direction, while a dome roof accelerates the flow consistently in all wind directions. Additionally, Aliabadi et al. [31] showed that an active roof-level roughness design can improve thermal comfort and air quality in the canyon for specific times of the day. These studies point to the role of architectural elements on urban ventilation, and draw attention to urban architecture as an adaptation method to urban environmental concerns.

As architectural elements, wind towers and wind catchers have been prevalent as historical designs in the Middle East and North Africa [32,33]. They are effective as a passive cooling and natural ventilation method for the indoor/outdoor interface, although the airflow rate is strongly influenced by the geometry of the wind catchers and the wind direction [34,35]. In modern architecture, however, such architectural interventions are uncommon, and their performance in enhancing pedestrian-level wind speed has not been fully evaluated. We aim to address this gap and study the effect of a wind catcher on urban ventilation in two-dimensional (2D) and three-dimensional (3D) urban street canyons.

The structure of the paper is illustrated as a flowchart in Figure 1. First, we introduce a simplified form of a wind catcher as an architectural intervention and present a robust assessment of this element in a water channel (Sections 2 and 3). The impact of a wind catcher on flow enhancement is compared to idealized 2D urban street canyons, as well as other architectural elements such as step-up/step-down canyons. Second, we use the experimental results to evaluate and validate a CFD model (Section 4), which is then used for visualizing the detailed flow fields. The CFD model is used to extend the analysis to 3D urban street canyons and improve the design of a wind catcher. Conclusions, limitations, and future work are discussed in Section 5.

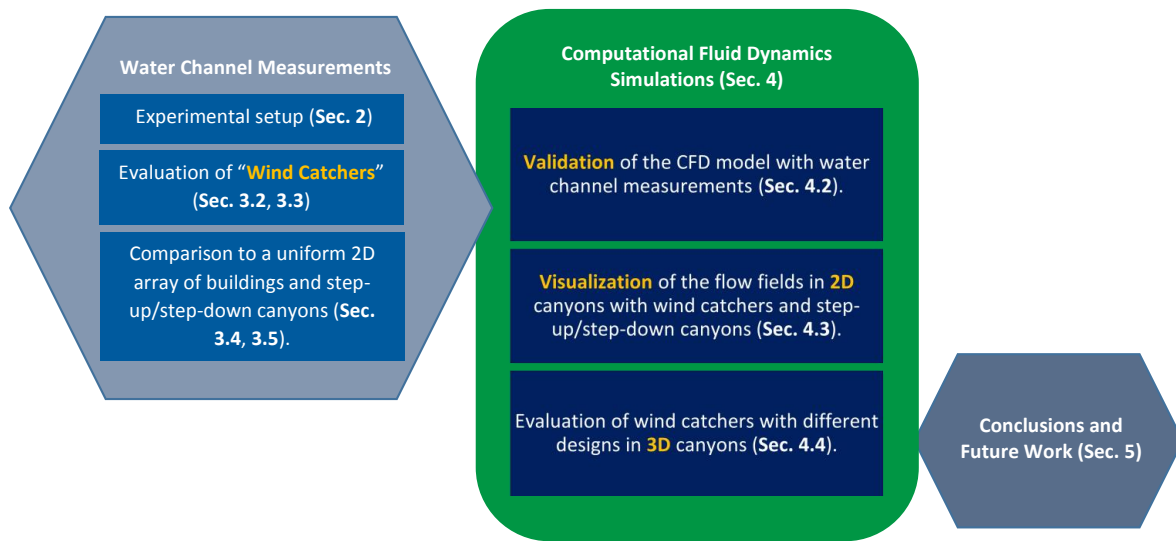


Figure 1. The flow chart and methodology of the current study.

2. Experimental Setup

A recirculating water channel in the Hydraulic Engineering Laboratory at the Department of Civil and Environmental Engineering, National University of Singapore, was used for all experiments. The sketch in Figure 2 shows the side view of the water channel. The water channel is 15 m long, 0.6 m tall and 0.6 m wide. High flow velocity at the test section was needed in some of the experiments, thus a partition made of marine plywood was installed to reduce the effective width from 0.6 m to 0.3 m at the test section. The test section measured 3.6 m long, 0.6 m tall and 0.3 m wide. The models of buildings spanned across the whole width of the test section, simulating flow across 2D urban street canyons (“canyons” hereafter), as shown in Figure 3. Flow straighteners made with a combination of plastic tubes, wire mesh and honeycomb minimize span-wise and vertical velocity components at the inlet. Two layers of ceramic marbles (0.5 inch or 1.27 cm diameter) accelerate the flow profile development such that the flow profile is fully developed at the test section. Far downstream of the water channel, an adjustable floodgate controls the water level. The water is circulated back to the tank with a pump. The flow rate was controlled by turning the valve and measured by a digital flowmeter. The maximum flow rate is 50 L/s. Acoustic Doppler Velocimeters, ADV (Vectrino by Nortek AS, Oslo, Norway), were used throughout the experiments to measure flow velocities. The ADV can measure all three components (stream-wise, vertical and span-wise) of velocities and velocity fluctuations up to 200 Hz. The accuracy is $\pm 0.5\%$ of measured value ± 1 mm/s. The ADV was mounted on metal frames with its vertical position adjustable. Although ADV is categorized as an intrusive measurement device, comparison with Laser Doppler Velocimeter (LDV, which is non-intrusive) measurements in Li et al. [36] verifies that our ADV probes did not disrupt the flow. Measurements taken by ADV and LDV are discussed in detail in Section 3.1.

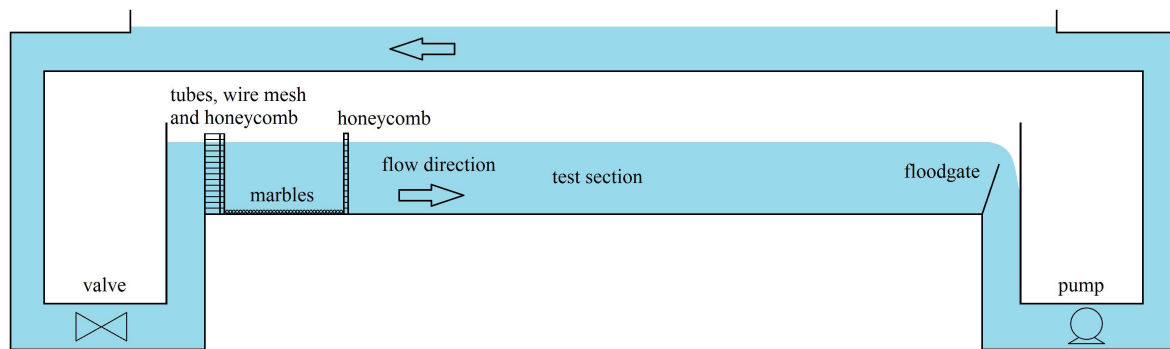


Figure 2. Side view of the recirculating water channel with an adjustable floodgate and a control valve to vary the flow rate and water level. The model blocks are placed at the test section, which is at the middle of the water channel.



Figure 3. Arrangement of model blocks in the test section to form seven canyons of aspect ratio 1 with height, $H = 12$ cm.

Table 1 summarizes four sets of experiments conducted: (i) the reference case, (ii) wind catcher, (iii) wind catcher in a reversed flow direction, and (iv) step-up and step-down canyons. In case (i), eight pieces of 12 cm tall \times 10 cm wide \times 30 cm long wooden blocks were spaced 12 cm apart from each other to simulate an array of 12 cm \times 12 cm canyons of aspect ratio 1, as shown in Figure 3. For case (ii) and case (iii), the dimension of the scaled-down prototype of the wind catcher is shown in Figure 4. The fourth canyon, or canyon 4, is the target canyon, for which we aim to enhance the near-ground flow. Therefore, the wind catcher (and the reversed wind catcher) is installed above canyon 4. For case (iv), the fifth model block is replaced by a taller block (44% taller) to simulate a step-up (i.e., taller downwind building) canyon 4 and a step-down (i.e., shorter downwind building) canyon 5. The Reynolds number, Re , is defined as $Re = U_{ref}H/\nu$, where U_{ref} is a reference velocity, H the canyon height and ν the kinematic viscosity. In all cases, the Reynolds numbers were above 10,000 to achieve fully turbulent regime [37–39]. The water depth was $3.4H$ for case (i) and $3.8H$ for cases (ii)–(iv).

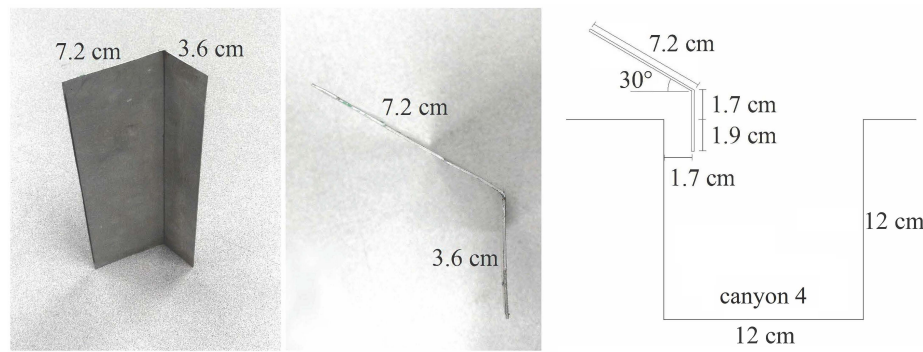


Figure 4. Photos and the dimensions of the wind catcher prototype.

Table 1. Summary of cases studied in the water channel. Case (i) represents the reference case with canyons of aspect ratio 1, cases (ii)–(iv) demonstrate the architectural interventions evaluated in this analysis. The middle-canyon profiles of all cases were measured in canyons 3–6 indicated by the dashed line shown in case (i) (not shown in cases (ii)–(iv) for clarity).

Case	Experimental setup
i Reference	
ii Wind catcher	
iii Reversed wind catcher	
iv Step-up/step-down canyons	

3. Experimental Results

This section discusses the experimental results for all four cases in Table 1. All three components of velocity were measured, but the mean span-wise velocity is zero, so only the mean stream-wise velocity, u , the mean vertical velocity, w , the stream-wise fluctuation, u' , and the vertical fluctuation, w' , are plotted. The mean velocities are time-averaged, while the velocity fluctuations are the root-mean-squared deviations from the mean (i.e., the standard deviation). All velocity components are normalized by a reference velocity, U_{ref} . In the literature, U_{ref} is either taken as the velocity at the roof level or the free-stream velocity. The velocity at the roof level is conveniently available but is very sensitive to the uncertainty in measurement position due to a large velocity gradient. On the other hand, the free-stream velocity remains relatively constant. For example, in a canyon with height H , the velocity at $0.1H$ above the roof level ($z/H = 1.1$, where z is the vertical distance from the ground) differs by about 50% compared to the velocity at the roof level ($z/H = 1.0$). In contrast, the difference between the velocity at $z/H = 2$ and $z/H = 3$ is less than 2% [36]. Kastner-Klein et al. [40] and

Li et al. [36] proposed taking the velocity at $z/H = 2$ or higher as the reference velocity, since it is less sensitive to the measurement position. We adopted their recommendation in this study by taking the free-stream velocity as U_{ref} .

3.1. Reference Case with Canyons of Aspect Ratio 1

Canyons with a unity aspect ratio (case (i) in Table 1) have been studied extensively in the literature, both experimentally [36,38,39,41] and numerically [31,42–44]. We repeated the measurements of this reference case to verify that our experimental setup can reproduce the results in the literature. We measured the middle-line velocity profiles of canyons 3–6 (indicated as the dashed lines in Table 1). The measurement frequency was 50 Hz and the measurement period was 60 s. Two separate sensitivity tests were conducted (one with double measurement frequency and the other with double measurement period) and verified that 50 Hz and a 60 s measurement period were sufficient. The eddy turnover time can be estimated as $H/U_{ref} \approx 0.7$ s, where $H = 0.12$ m and $U_{ref} = 0.17$ m/s. Therefore, the averaging period was about two orders of magnitude larger than the eddy turnover time. The flow was let to settle for 20 min (>1500 eddy turnover time) to ensure stationary before taking measurements. To confirm the repeatability of the experimental setup, three sets of measurements were taken on three separate days. The pump was turned off and the water was allowed to drain off after each set of measurement, i.e., each set of experiment was a new start by turning on the pump and allowing the flow to settle for 20 min before measurements. The three runs produced negligibly small run-to-run standard deviations: 0.001 m/s for the mean velocities and 0.0005 m/s for the velocity fluctuations, confirming the repeatability of the experimental setup.

The in-canyon profiles of canyons 3–6 are identical. This means that the flow has developed into the urban roughness flow at canyon 3, in agreement with Brown et al. [41] and Meroney [38]. For this reference case, since the velocity profiles in canyons 3–6 are similar, we plot only the profiles of canyon 4 in Figure 5. All profiles are normalized by U_{ref} . The result in Li et al. [36] serves as a benchmark comparison. This study used Acoustic Doppler Velocimeter (ADV) and had an $Re = 19,000$, while Li et al. [36] used Laser Doppler Velocimeter (LDV) and had an $Re = 11,000$. The good agreement between both studies verifies that the ADV in our experiments did not disrupt the flow. In addition, Li et al. [36] only measured up to $z/H = 1.2$, and we extended the measurement to $z/H = 2.5$ to check at what elevation the flow recovers to the free-stream velocity. Figure 5a shows that at z/H about 2, the stream-wise velocity approaches the free-stream velocity. Near the ground level, u/U_{ref} has a magnitude up to 30% in the negative x -direction. The magnitude of u/U_{ref} decreases almost linearly with increasing z/H to zero at the mid-canyon height ($z/H = 0.5$), then increases to 30% at the roof level ($z/H = 1.0$). On the other hand, Figure 5b shows that w/U_{ref} has a magnitude up to 10% at the mid-canyon height. Near the ground and above the canyon, w/U_{ref} are negligible. For turbulence, Figure 5c,d show that both u'/U_{ref} and w'/U_{ref} are the highest near the roof level and decay with increasing distance from the roof. This is expected, as most turbulence is generated at the roof level, where the velocity gradient is the highest. Inside the canyon ($z/H < 1$), u'/U_{ref} and w'/U_{ref} stay relatively constant at about 5%. The mean span-wise velocity (not shown) was zero throughout, indicating the 2D nature of the flow.

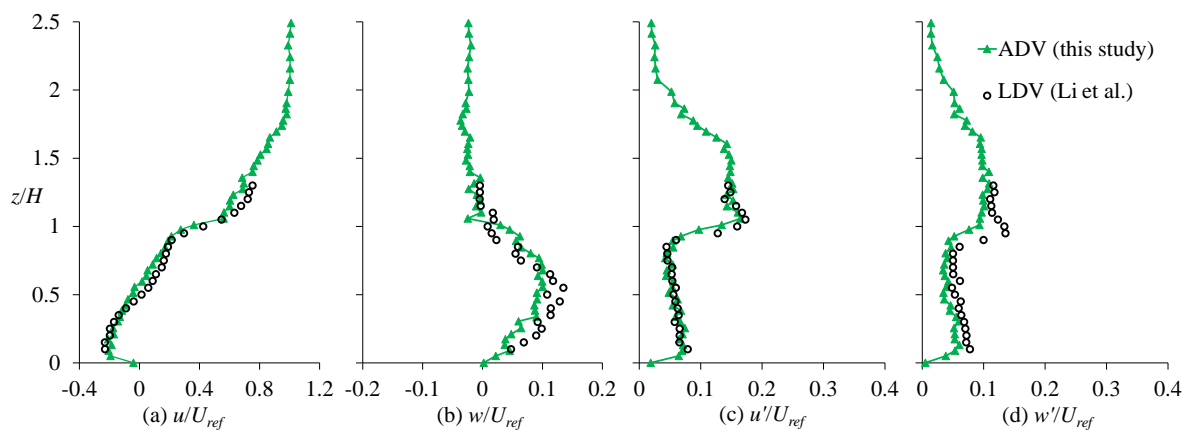


Figure 5. Normalized middle-line velocity profiles at canyon 4 measured with Acoustic Doppler Velocimeter (ADV, this study) and Laser Doppler Velocimeter (LDV, from Li et al. [36]). (a) mean stream-wise velocity, (b) mean vertical velocity, (c) stream-wise velocity fluctuation, and (d) vertical velocity fluctuation.

3.2. Canyons with a Wind Catcher

Next, we added a wind catcher above canyon 4, without changing the arrangement of the model blocks (case (ii) in Table 1). Similar to the reference case, the measurement frequency was 50 Hz and the measurement period was 60 s. To speed up the measurement process, U_{ref} was increased by about two times and, correspondingly, the measurement frequency was doubled to 100 Hz and the measurement period was halved to 30 s. Both sets of experiments produced similar results, so only the latter (100 Hz and 30 s measurements) is reported. We are interested in quantifying the effect of the wind catcher in the target canyon 4, the upstream canyon 3, and the downstream canyons 5 and 6.

Figure 6a shows that u/U_{ref} is distinctive in canyon 4 compared to the other canyons. First, u/U_{ref} in canyon 4 is positive below the mid-canyon height ($z/H < 0.5$) while the other canyons have negative u/U_{ref} . Second, near the ground level, u/U_{ref} in canyon 4 is about 2.5 times larger in magnitude compared to the other canyons. Third, u/U_{ref} approaches zero near $z/H = 0.7$, and becomes negative at $z/H > 0.7$. This suggests a strong counter-clockwise vortex in canyon 4, with the vortex core located near $z/H = 0.7$. This is caused by the protrusion of the wind catcher above the roof level, which induces additional blockage to the flow upstream. Based on the geometry in Figure 4, the protrusion of the wind catcher is 5.3 cm above the roof level. The canyon height is 12 cm, so the effective blockage to the flow is 12 cm + 5.3 cm = 17.3 cm. In contrast to a counter-clockwise vortex in canyon 4, negative u/U_{ref} below $z/H = 0.5$ implies that clockwise vortices form in canyons 3, 5, and 6. The normalized vertical velocity, w/U_{ref} , remains small (<10%) in canyons 3, 5, and 6, as shown in Figure 6b. Between $z/H = 0.7$ and $z/H = 1.5$, canyon 4 has higher negative w/U_{ref} of up to 10%, possibly induced by the wake of the wind catcher. Concerning turbulence, Figure 6c,d show that overall, u'/U_{ref} is larger than w'/U_{ref} . Near the ground level ($z/H < 0.2$), u'/U_{ref} in canyon 4 is twice as high compared to the other canyons. Above canyon 4, the maximum u'/U_{ref} and w'/U_{ref} are recorded near $z/H = 1.4$, which is the protrusion height of the wind catcher. These high velocity fluctuations travel downstream so canyons 5 and 6 record higher u'/U_{ref} and w'/U_{ref} compared to canyon 3, which is upstream of the wind catcher.

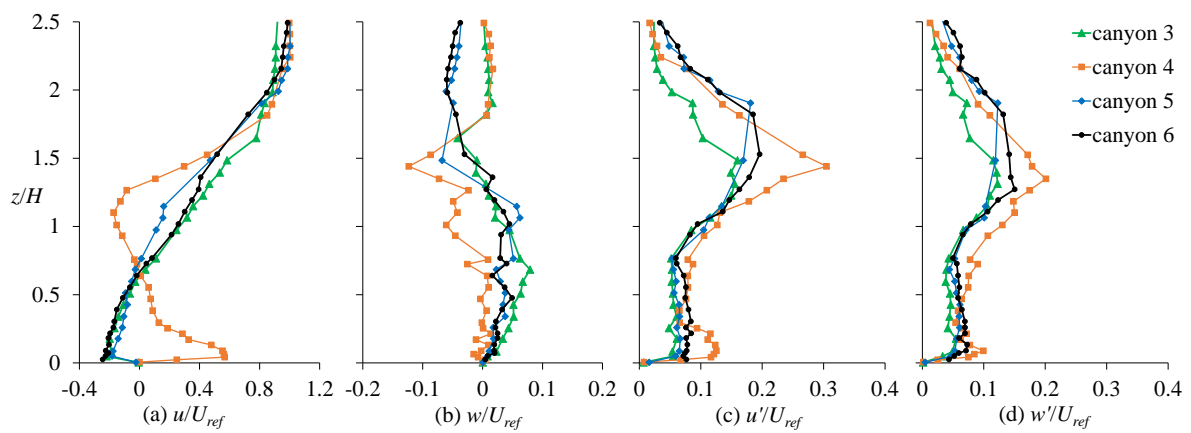


Figure 6. Normalized middle-line velocity profiles of canyons 3–6 with a wind catcher above canyon 4. (a) mean stream-wise velocity, (b) mean vertical velocity, (c) stream-wise velocity fluctuation, and (d) vertical velocity fluctuation.

3.3. Wind Catcher in a Reversed Flow Direction

A wind catcher can be installed with its inlet oriented towards the prevailing wind direction to maximize the flow enhancement in a canyon. If the wind comes at an opposite direction (e.g., diurnal wind where the wind changes direction at night), a wind catcher becomes a “reversed wind catcher”, depicted as case (iii) in Table 1. In this setting, canyon 4 is still the target canyon, as the wind catcher is nearest to canyon 4. The measurement frequency and period were 100 Hz and 30 s. Figure 7 summarizes the middle-line velocity profiles of canyons 3–6 with a reversed wind catcher. The flow profiles of canyons 3 and 4 are similar to those in the reference case, showing that the reversed wind catcher has little effect on the upstream canyon 3 and the target canyon 4. In canyon 5, u/U_{ref} drops to nearly zero throughout the canyon. The wake induced by the protrusion of the reversed wind catcher above the roof level is apparent at canyon 5, as the magnitude of u/U_{ref} remains small up to $z/H = 1.4$. Above $z/H = 1.4$, u/U_{ref} increases rapidly to recover to the free-stream velocity. In canyon 6, near-ground u/U_{ref} recovers to about 20%, slightly lower compared to canyon 4. Concerning turbulence, Figure 7c,d show that u'/U_{ref} is larger than w'/U_{ref} , consistent with all previous cases. In canyons 3, 4, and 6, both u'/U_{ref} and w'/U_{ref} are between 5% and 10%, except near the ground level, where they decay to zero. Canyon 5 records the smallest u'/U_{ref} and w'/U_{ref} at about 2% inside the canyon.

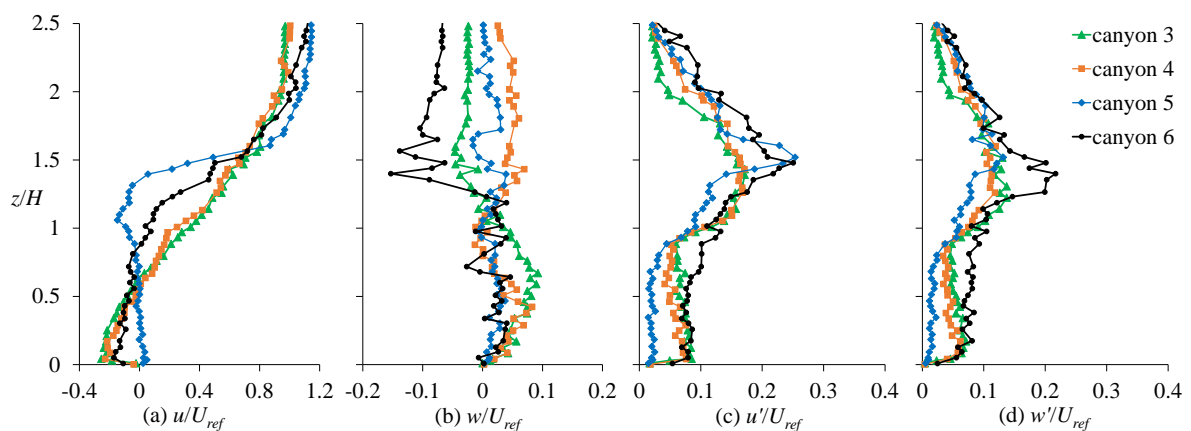


Figure 7. Normalized middle-line velocity profiles of canyons 3–6 with a reversed wind catcher above canyon 4. (a) Mean stream-wise velocity, (b) mean vertical velocity, (c) stream-wise velocity fluctuation, and (d) vertical velocity fluctuation.

3.4. Step-Up/Step-Down Canyons

The wind catcher captures atmospheric wind with an inlet protruding above the roof level, where the wind speed is higher due to less obstruction to flow. The wind catcher in case (ii) protrudes 5.3 cm above the roof level of a 12 cm tall canyon. Does a taller building with an equivalent height induce similar flow enhancement effect in canyon 4? We attempt to answer this question by studying flows across step-up and step-down canyons (case (iv) in Table 1). In this experiment, the fifth building model was 17.3 cm tall (to match the effective blockage height of the wind catcher in case (ii)), while all other building models remained at 12 cm tall. Canyon 4 is a step-up canyon, while canyon 5 is a step-down canyon. The measurement frequency and period were 100 Hz and 30s. Figure 8 summarizes the experimental results.

Figure 8a shows that canyon 5 records almost zero flow, while canyons 3, 4, and 6 have about the same u/U_{ref} profiles inside the canyons. These profiles are similar to the u/U_{ref} profiles in the case of a reversed wind catcher in Figure 7a. This means that the tall building obstructs the flow in a similar fashion as the reversed wind catcher. The profiles of w/U_{ref} are also comparable across different canyons, except above canyon 4. Compared to the reversed wind catcher (Figure 7b), Figure 8b shows that w/U_{ref} above canyon 4 is slightly higher in this case. This may be due to the geometry of the blockage. In the case with a reversed wind catcher, the flow above canyon 4 has a milder turn of 30 degrees when it approaches the sloped plate of the reversed wind catcher. In the case with a tall building downwind of canyon 4, the flow approaching building 5 (the downwind building of canyon 4) turns 90 degrees to align with the vertical windward wall of building 5. The abrupt turning of 90 degrees induces a higher w/U_{ref} compared to a milder turn of 30 degrees in the case with a reversed wind catcher. Concerning turbulence, Figure 8c,d are similar to Figure 7c,d, further suggesting that a taller building obstructs the flow similarly to a reversed wind catcher.

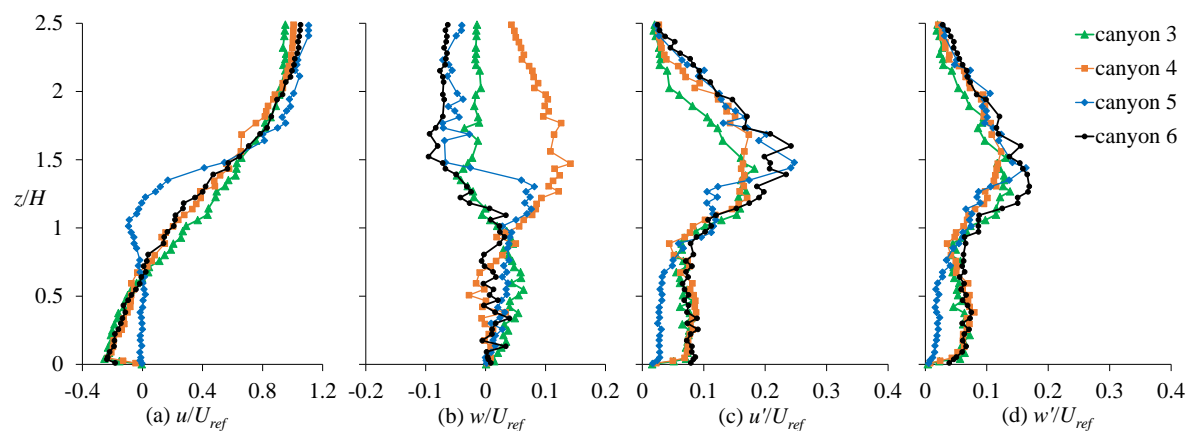


Figure 8. Normalized middle-line velocity profiles of canyons 3–6 with a step-up canyon 4 and a step-down canyon 5. (a) mean stream-wise velocity, (b) mean vertical velocity, (c) stream-wise velocity fluctuation, and (d) vertical velocity fluctuation.

3.5. Comparison between Wind Catcher, Reversed Wind Catcher, and Step-Up/Step-Down Canyons

Figure 9 plots the velocity profiles in canyons 3–6, comparing the three types of architectural interventions to the reference case with canyons of aspect ratio 1. Since w/U_{ref} is small near the ground level, only $|u|/U_{ref}$ is plotted (the absolute values are taken to ease comparison, since the reference case has negative u/U_{ref} near the ground level). To focus on the pedestrian-level wind speed, the y -axis ranges up to the mid-canyon height at $z/H = 0.5$ (instead of $z/H = 2.5$). Figure 9a shows that none of the three architectural interventions affects near-ground wind speed in the upstream canyon 3. Figure 9b shows that in the target canyon 4, the reversed wind catcher and the tall building have no effect, while the wind catcher enhances near-ground wind speed by more than 2.5 times.

Figure 9c shows that the tall building and the reversed wind catcher reduce the flow to nearly zero in the downstream canyon 5, while the wind catcher has negligible effect. Lastly, Figure 9d shows that in the further downstream canyon 6, all cases have about the same near-ground wind speed, except the case with a reversed wind catcher, which has a slightly lower speed.

In summary, the wind catcher is shown to be effective in channeling atmospheric wind into a target canyon. A reversed wind catcher does not enhance flow in the target canyon and reduces flows into downstream canyons. This drawback of wind speed reduction in an unfavorable wind direction can be overcome with improved designs such as incorporating a rotatable inlet. Similar to a reversed wind catcher, a tall building amid an array of lower buildings does not enhance flow in the target canyon and reduces flow in the immediate downstream canyon.

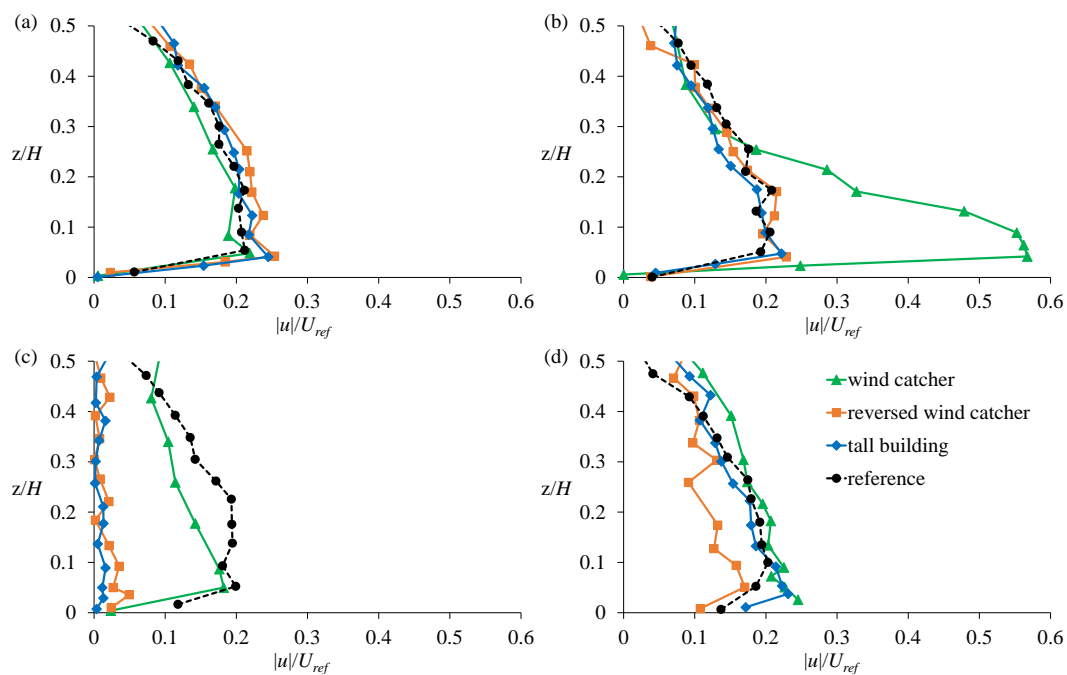


Figure 9. Normalized (absolute) stream-wise velocity comparing the cases with a wind catcher, a reversed wind catcher, and step-up/step-down canyons with reference to canyons of aspect ratio 1 in: (a) canyon 3, (b) canyon 4, (c) canyon 5, and (d) canyon 6.

4. CFD Simulations

We repeated the studies of all experimental cases with CFD simulations. Both the experimental and computational approaches have their strengths and weaknesses [45,46]. We could not perform flow visualization with our experimental setup because the partition walls were not transparent. A validated CFD model serves as a valuable tool to complement this drawback of experiment, as the CFD result can reveal the holistic flow fields. We also need CFD simulations to study the flow across a real-scale built environment, since full-scale building models will not fit even in the largest wind tunnel and water channel. We conducted CFD simulations at both the experimental scale (i.e., reduced scale) and full scale to justify the scale reduction in our water channel experiments.

4.1. Numerical Model

We used ANSYS DesignModeler (Release 17.2) for geometrical modelling and ANSYS Meshing (ANSYS Inc., Canonsburg, PA, USA) [47] for mesh generation. The CFD domain had similar geometrical dimensions as the experimental setup, except the span-wise length was reduced to H with a periodic boundary condition in the span-wise direction to reduce the total number of grids

[31,48–50]. The top face had a symmetric boundary condition. The domain height was $3.4H$ or $3.8H$, which corresponded to the water depth in the experiments. A sensitivity study with $10H$ domain height showed that the mean stream-wise velocity was smaller for $1 < z/H < 2$, but had no effect in the canyon ($z/H < 1$). The inlet, located $4H$ from the first model block, was prescribed with the velocity profile measured in the experiments at the same location. The outlet, located $15H$ from the last block [51], had a zero-gradient boundary condition. All walls including the bottom had a no-slip boundary condition. In the experiments, all model blocks were coated with epoxy, which smoothed the surfaces and all walls in the CFD domain were set to be smooth. Figure 10 shows an example of the mesh for the reference case. The model had 2.5 million grids in total. The canyons had a fine mesh resolution with uniform grid size $H/60$. The same resolution was maintained above the roof level up to $1.8H$. Above $1.8H$, the mesh was coarsened. Similarly, the mesh was coarsened upstream of the first building and downstream of the last building (not shown). The maximum mesh expansion ratio was 1.2. The span-wise direction had 25 uniform grids.

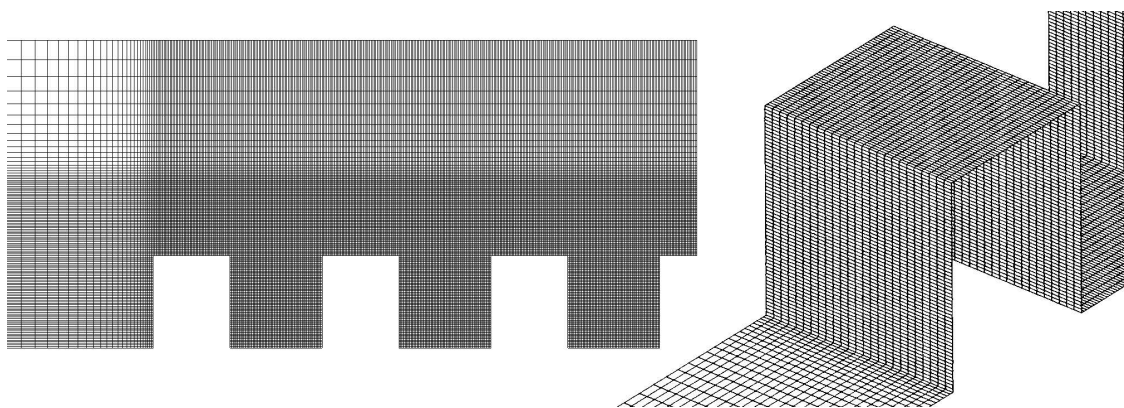


Figure 10. Side view of the central plane (only the first three canyons shown) and 3D view (only the first model block shown) of the Computational Fluid Dynamics domain.

The open-source, finite volume solver Open Field Operation and Manipulation (OpenFOAM), was adopted for CFD simulations. All simulations were run with OpenFOAM version 3.0.1 (OpenCFD Ltd., Bracknell, UK) [52] in the Linux platform Ubuntu 15.10, (Canonical Ltd., London, UK) in a Dell Precision Tower 7910 Workstation (Dell Inc., Round Rock, TX, USA) with 48 processors. Up to 46 processors were used for a single run, depending on the number of grids in the mesh. We used the built-in Reynolds-averaged Navier–Stokes (RANS) solver, “simpleFOAM”, which is a steady-state solver for incompressible turbulent flow with SIMPLE (Semi-Implicit Method for Pressure Linked Equations) pressure-velocity coupling and $k-\epsilon$ turbulence closure. There are three commonly used $k-\epsilon$ closure schemes: standard $k-\epsilon$, Re-Normalization Group (RNG) $k-\epsilon$, and realizable $k-\epsilon$. Hang et al. [7] recommends the standard $k-\epsilon$ scheme over the RNG $k-\epsilon$ scheme, as the former agrees better with their experimental results. We tested the standard $k-\epsilon$ and realizable $k-\epsilon$ schemes and found that the former agrees better with our experimental results. Therefore, the standard $k-\epsilon$ was adopted for all our simulations. Second order Gaussian integration with linear interpolation was used for all gradient schemes and divergence schemes. All Laplacian schemes were based on Gaussian integration with linear interpolation and non-orthogonal correction. The standard wall function was employed to reduce computational cost by allowing a coarser mesh. The tolerance of residuals was set at 10^{-5} for all parameters, and iterations were continued until all residuals reach a plateau (do not change with further iterations) [53]. Post-processing was done with the open-source software ParaView version 5.3.0 (Kitware Inc., Clifton Park, NY, USA) [54].

4.2. Simulation of the Reference Case

We first look at simulation results of the reference case with canyons of aspect ratio 1. The reduced-scale experiment had a canyon height, $H = 12$ cm, and a corresponding Reynolds number, $Re = 19,000$. In a real-scale built environment, Re is much higher. For example, a 3 m/s wind flow across a 20 m tall canyon has an $Re = 3.8 \times 10^6$. Such a high Re cannot be achieved in reduced-scale experiments so we need to use CFD simulations for full-scale studies. Two CFD simulations were run: one with $H = 12$ cm with reference velocity, $U_{ref} = 0.52$ m/s in water ($Re = 62,000$); another one with $H = 20$ m with $U_{ref} = 3$ m/s in air ($Re = 3.8 \times 10^6$) to simulate a real-scale built environment. In addition, a full-scale simulation with a refined mesh (with twice the resolution in all three directions) was run to check for mesh independence. Figure 11 compares numerical and experimental results. Since canyons 3–6 have similar velocity profiles, only the velocity profiles at canyon 4 are plotted.

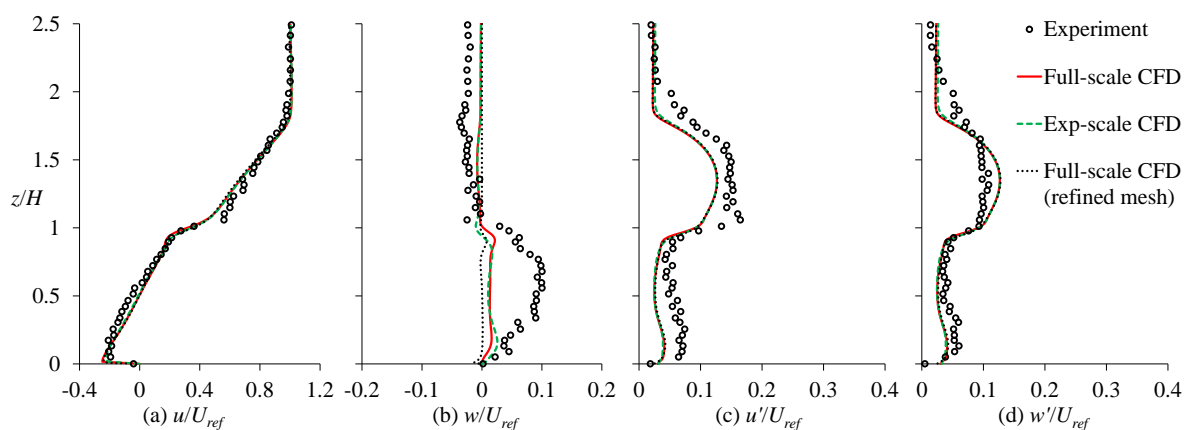


Figure 11. Normalized middle-line velocity profiles at canyon 4 comparing experimental and CFD results for the reference case. (a) mean stream-wise velocity, (b) mean vertical velocity, (c) stream-wise velocity fluctuation, and (d) vertical velocity fluctuation. “Exp-scale” and “Full-scale” are experimental scale and real scale in a built environment.

Overall, the full-scale CFD simulation produced results similar to the reduced-scale CFD simulation, verifying that the reduced-scale CFD simulation (and the reduced-scale experiment) is representative of flows across full-scale built environments. The flow pattern does not change when increasing Re from 19,000 to 62,000 and further to 3.8×10^6 , suggesting that Reynolds independence is achieved at $Re > 10,000$ [37–39]. Compared to experimental data, Figure 11a shows a satisfactory agreement of u/U_{ref} at both scales. Nevertheless, Figure 11b shows that the CFD simulations under-predicted w/U_{ref} at both scales. Figure 11c,d show that above the roof level ($z/H > 1$), both u'/U_{ref} and w'/U_{ref} agree well with the experiment. Inside the canyon ($z/H < 1$), CFD simulations predicted lower turbulence. Note that the $k-\epsilon$ turbulence closure scheme produces isotropic turbulence so u'/U_{ref} equals w'/U_{ref} in the CFD simulations. Lastly, refining the mesh produced similar results, hence mesh independence is achieved. Quantitative evaluations of model validation and mesh independence are provided in Appendix A.

4.3. Simulations of Cases with Different Types of Architectural Interventions

This section discusses CFD model validation of the cases with the three types of architectural interventions: a wind catcher, a reversed wind catcher, and step-up/step-down canyons. Figure 12 plots the u/U_{ref} profiles of canyons 3–6 for the three cases. The experimental results are plotted as filled circles, while the CFD results are plotted as solid lines. For brevity, only u/U_{ref} profiles are plotted (the profiles of w/U_{ref} , u'/U_{ref} and w'/U_{ref} in selected canyons are plotted and discussed later in this section). All three cases show good agreement between experimental and simulation results.

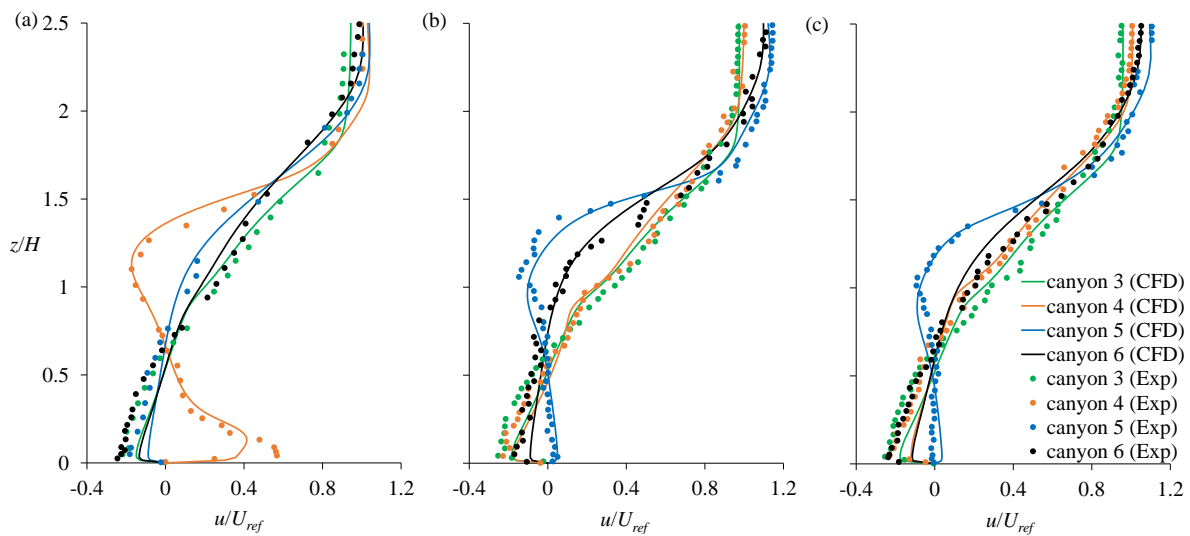


Figure 12. CFD model validation with experiments for the cases of (a) wind catcher, (b) reversed wind catcher, and (c) step-up/step-down canyons.

Similar to the reference case, we conducted CFD simulations at reduced scale (Re in the order of 10^4) and full scale (Re in the order of 10^6). Figure 13 plots the profiles of u/U_{ref} , w/U_{ref} , u'/U_{ref} , and w'/U_{ref} in canyon 4 for the case with a wind catcher. The CFD simulations are able to predict the trends of both the mean velocities and the velocity fluctuations observed in the experiment. Although Re differs by two orders of magnitude, the normalized velocity profiles at full scale coincide with the profiles at experimental scale, justifying that the reduced-scale experiment can reproduce the flow patterns with a wind catcher in a full-scale built environment. Similarly, Figure 14 plots the velocity profiles in canyon 5 for the case with a reversed wind catcher at both the experimental scale and full scale. Note that canyon 5 is selected because the flow profiles in canyon 5 are the most distinctive in the case with a reversed wind catcher. The CFD simulations are able to predict the trends of both the mean velocities and the velocity fluctuations observed in the experiment. The velocity profiles for the case of step-up/step-down canyons are not shown here, as they are quite similar to the profiles in Figure 14. Quantitative evaluations of model validation are provided in Appendix A.

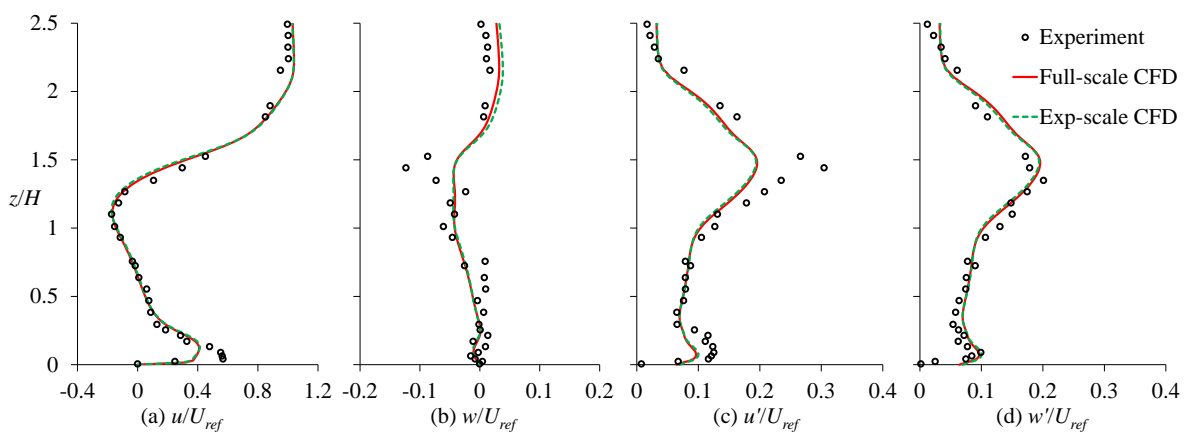


Figure 13. Normalized middle-line velocity profiles at canyon 4 comparing experimental and CFD results for the case with a wind catcher. (a) mean stream-wise velocity, (b) mean vertical velocity, (c) stream-wise velocity fluctuation, and (d) vertical velocity fluctuation. “Exp-scale” and “Full-scale” are experimental scale and real scale in a built environment.

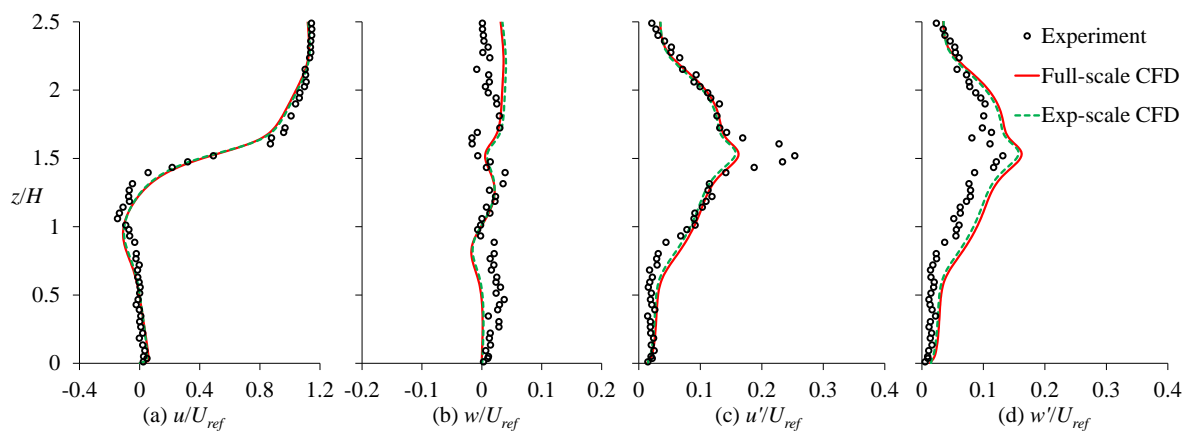


Figure 14. Normalized middle-line velocity profiles at canyon 5 comparing experimental and CFD results for the case with a reversed wind catcher. (a) Mean stream-wise velocity, (b) mean vertical velocity, (c) stream-wise velocity fluctuation, and (d) vertical velocity fluctuation. “Exp-scale” and “Full-scale” are experimental scale and real scale in a built environment.

To visualize the flow patterns in all simulated cases, Figure 15 plots the middle-plane normalized velocity magnitude (U_{mag}/U_{ref}) contours and vectors of canyons 3–6. For the reference case, Figure 15a shows that all canyons exhibit identical flow fields with a large clockwise-rotating vortex in each canyon. Each vortex has its core near the center of the canyon. The maximum near-ground velocity is about 25% of the free-stream velocity.

For the case with a wind catcher, Figure 15b reveals how the wind catcher channels atmospheric wind into the target canyon 4. Atmospheric wind captured at the inlet increases its momentum while squeezing through the narrowing channel between the roof and the top plate of the wind catcher. The high-speed jet exiting the outlet of the wind catcher travels vertically downward and turns into the stream-wise direction upon impinging the ground, boosting wind speed at the pedestrian level. This jet then turns again and moves up along the windward wall, before exiting to the atmosphere. The positively upward flow along the windward wall and the negatively downward flow along the leeward wall induces a strong counter-clockwise vortex, as opposed to clockwise vortices formed in canyons 3, 5, and 6. The cores of the vortices in canyon 4 and canyon 5 are located at around $z/H = 0.7$.

For the case with a reversed wind catcher, Figure 15c shows that the flow field in canyon 4 is not altered by the reversed wind catcher, except near the top right corner, where flow escapes through the “outlet” of the reversed wind catcher. The reversed wind catcher is installed near the windward wall so it has little effect on the velocity profiles at the middle line of the canyon. This explains the similarity between the velocity profiles of canyon 3 and canyon 4 measured in the experiment. The protrusion of the reversed wind catcher above the roof level induces a horizontally-elongated separation bubble, which spans above canyon 5. This separation bubble inhibits atmospheric wind from flowing into canyon 5, causing canyon 5 to be quiescent. Further downstream at canyon 6, part of the atmospheric flow is able to enter canyon 6, but the velocity magnitude is lower compared to canyon 3.

Lastly, for the case of step-up/step-down canyons, Figure 15d confirms that a tall building exhibits blockage effects similarly to a reversed wind catcher. The flow fields in canyons 3, 4, and 6 remain relatively unchanged compared to the reference case. In canyon 5, which is a step-down canyon, there is almost no flow at the pedestrian level due to blockage of the upstream tall building.

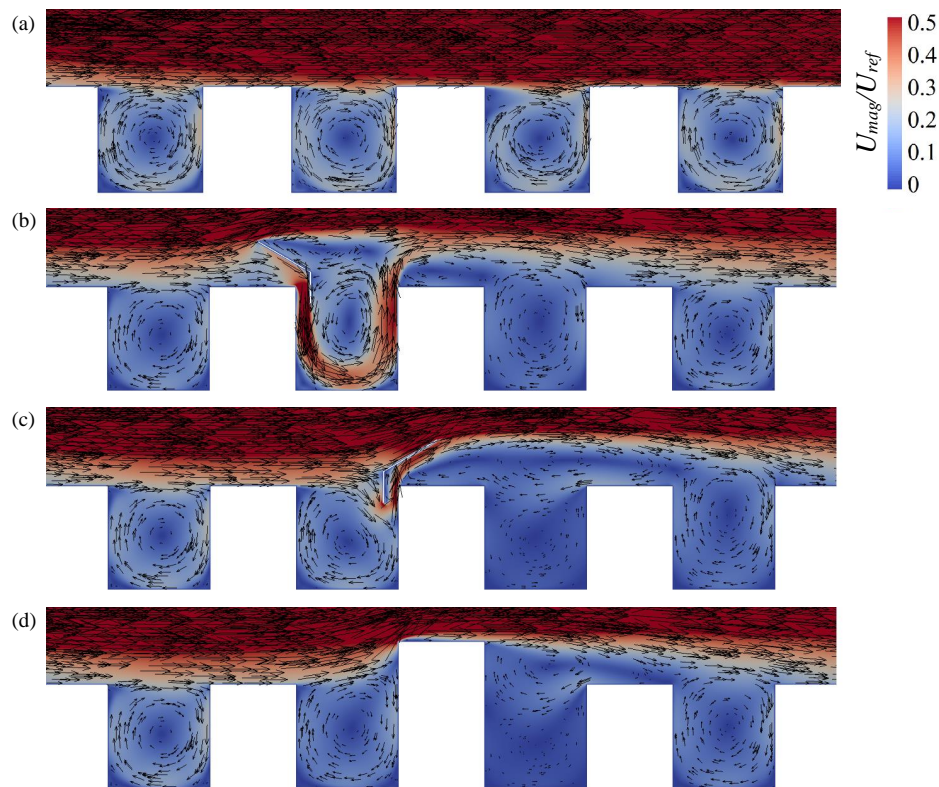


Figure 15. Normalized velocity magnitude contours and vectors in canyons 3–6 for cases: (a) reference case, (b) wind catcher, (c) reversed wind catcher, and (d) step-up/step-down canyons. The scale ranges from 0 to 0.5 (not 1.0) to emphasize the in-canyon flow.

4.4. Wind Catcher in 3D Canyons

All analyses discussed thus far are for 2D canyons. This section extends the study of wind catchers to 3D canyons with a finite building length. As our water channel has a limited width (30 cm), it is not suitable to study flow across 3D canyons. The wind tunnel experiment across nine arrays of twelve rectangular model blocks in Hang et al. [7] was used to validate our CFD model with 3D canyons. RANS with standard $k-\epsilon$ turbulence closure was adopted, with boundary conditions similar to that described in Section 4.1. Figure 16 compares CFD simulations with experimental results. The RANS simulation result in Hang et al. [7] is also included for comparison. Note that the CFD model in Hang et al. [7] employed a symmetric span-wise boundary condition while our CFD model employed a periodic span-wise boundary condition (we repeated the simulation with a symmetric span-wise boundary condition and obtained identical results so both boundary conditions are applicable in the span-wise direction). Overall, Figure 16 shows that both CFD simulations agree well with experiments, except the location of the peak turbulence kinetic energy. The CFD simulations predicted the peak near $x/B = 0$ while the experiment observed the peak near $x/B = 4$. For $x/B > 4$, the turbulence kinetic energy profiles from both CFD and experiment show a decreasing trend. Quantitative evaluations of model validation are provided in Appendix A.

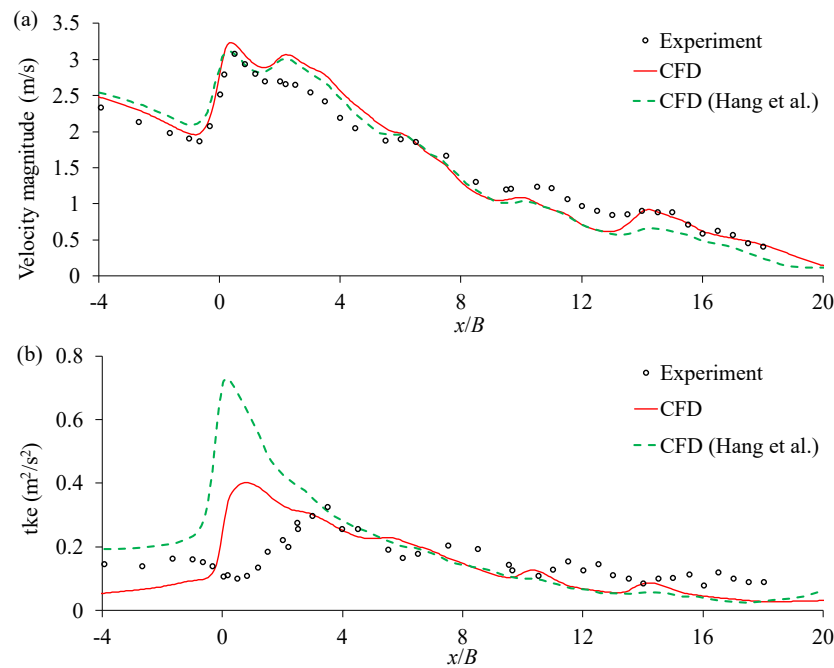


Figure 16. Along-street horizontal profiles of (a) velocity magnitude and (b) turbulence kinetic energy at elevation $z/B = 0.5$, where $B = 30$ mm is the building width. The x -axis is normalized by B , and $x/B = 0$ corresponds to the first building. Solid lines are from our CFD simulation, both the experimental data and the dashed-lines CFD are from Hang et al. [7].

Having validated the CFD model with 3D canyons, we simulated flow across wind catchers in 3D canyons, as depicted in Figure 17a. Both the height and the width of the canyons remain at H , while the span-wise building length is $5H/12$, representing narrow buildings commonly found in urban areas. Both the wind catcher span-wise length and the street width equal $5H/12$. As shown in Figure 17a, we modelled only one array of buildings. To represent an infinite array of buildings, we employed a periodic/symmetric boundary condition in the span-wise faces of the computational domain (i.e., the array repeats itself span-wise infinitely). The domain height and length, as well as the boundary conditions at the inlet, outlet, top, and walls are the same as outlined in Section 4.1. The canyons had a fine mesh resolution with uniform grid size $H/60$. The mesh was coarsened with a mesh expansion ratio (<1.2) at three regions: above $1.8H$, upstream of the first building, and downstream of the last building. The span-wise direction had uniform grid size $H/60$. Since the flow across 3D canyons behaves differently than the flow across 2D canyons, a new reference case with full-scale 3D canyons is simulated. The Re based on H is 2.0×10^6 . Figure 18 plots the magnitude of u/U_{ref} up to the mid-canyon height ($z/H = 0.5$), as we are interested in the pedestrian-level flows. In a 3D canyon, near-ground wind speed is small ($<10\%$ of the free-stream velocity). Installing a wind catcher boosts the near-ground wind speed to about 15%. Recall that a wind catcher in a 2D canyon boosts near-ground wind speed by 2.5 times. This means that the wind catcher is less effective in terms of pedestrian-level wind speed enhancement in 3D canyons. The velocity contour in Figure 17c reveals that the wind catcher captures high-speed atmospheric wind via its inlet, but the high-speed downward jet loses momentum before reaching the ground level. To understand what happens between the leeward wall and the vertical plate of the wind catcher, we plot the velocity contours of section A-A in Figure 17e. Note that, in Figure 17e, we plot the magnitude of span-wise velocity, v , and vertical velocity, w , but exclude the stream-wise velocity, u , to emphasize the span-wise flow. The magnitudes of v and w are normalized with U_{ref} . Right below the top plate of the wind catcher (the white line), part of the flow turns around the side edges of the plate. This flow near the side edges then either flows upward or turns around further to hit the top surface of the plate. This flow pattern

is induced by the pressure difference across the top plate of the wind catcher. The top surface of the plate has a low pressure due to flow separation, while the bottom surface has a high pressure due to impinging high-speed flow captured at the inlet. This pressure difference drives the span-wise leakage, analogous to an induced vortex at the wingtip of an airfoil. By sealing the sides of the wind catcher with sidewalls as shown in Figure 17b (as opposed to no sidewalls in Figure 17a, Figure 18 shows that near-ground u/U_{ref} increases to over 30%. The velocity contours in Figure 17d,f confirm that, by preventing the span-wise leakage with sidewalls, the high-speed jet captured at the inlet of the wind catcher travels downward with little momentum loss to the span-wise direction until it reaches the ground. It then turns into both the span-wise and the stream-wise directions. The flow that turns into the stream-wise direction is observed as the high-speed jet in Figure 18.

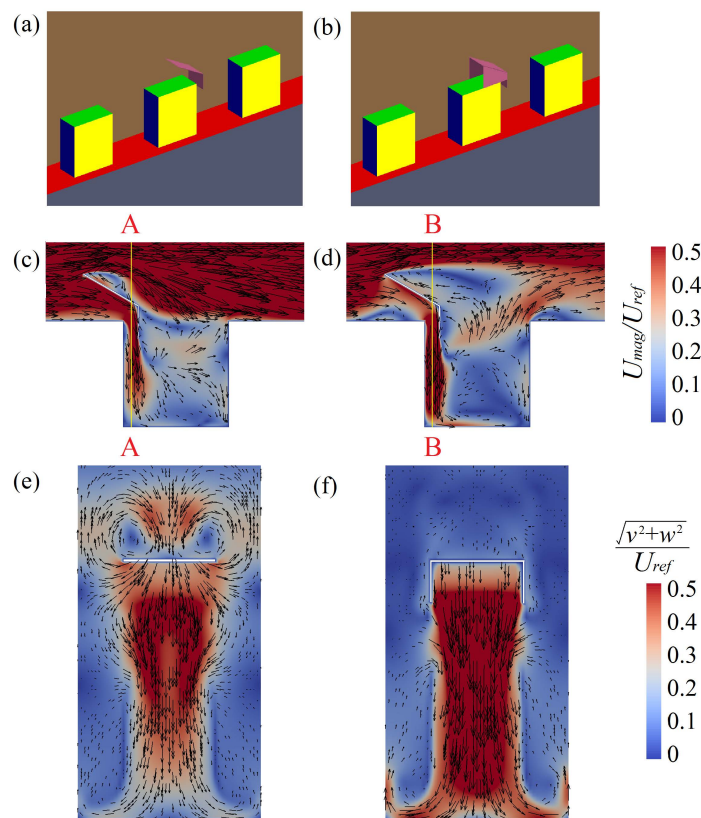


Figure 17. (a) Wind catcher and (b) wind catcher with sidewalls. Normalized velocity magnitude contours and vectors in canyon 4 for (c) wind catcher and (d) wind catcher with sidewalls. Normalized span-wise and vertical velocity contours and vectors of (e) section A-A and (f) section B-B.

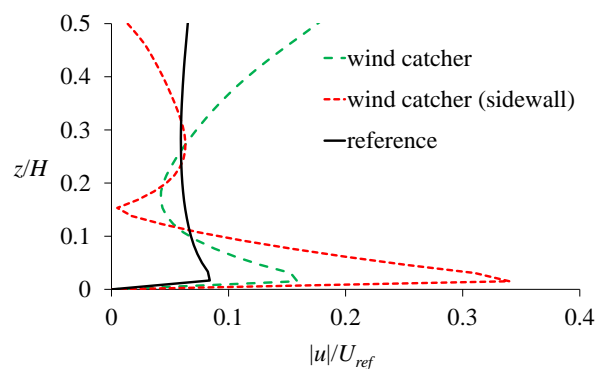


Figure 18. Comparison of normalized stream-wise velocity magnitude at the middle of canyon 4.

5. Conclusions

Urban ventilation is a key element in the microclimate of cities, as it alleviates several major environmental challenges such as air quality, thermal comfort, and urban heat island effect. Urban morphology and design are the major contributing factors to urban ventilation and should be taken into great consideration for new development or extensions of cities. In existing urban areas facing climate challenges, however, alternative solutions are needed. Architectural interventions that improve the natural ventilation of urban street canyons can be an example of such solutions.

The focus of this study is on the pedestrian-level ventilation in urban environments, and the role of architectural interventions such as wind catchers was evaluated. The strength of the current study is the comprehensive approach that (a) combines the experimental measurements with Computational Fluid Dynamics simulations of flow field with wind catchers, (b) extends the analyses to both 2D and 3D canyons, and (c) further compares the results with step-up/step-down canyons, as a representative of a tall building with a height equivalent to the wind catcher. The summary of our findings is as follows:

- We employed water channel measurements over an idealized array of 2D street canyons with an aspect ratio of 1 and evaluated the addition of a wind catcher in the aligned and reversed direction of the approaching wind. We found that a wind catcher significantly enhances pedestrian-level ventilation by increasing the local wind speed by 2.5 times. When installed in a reversed wind direction, however, the wind catcher acts similarly to a tall building with an equivalent height, such that the airflow in the downstream canyon is decreased. Therefore, further engineering analysis is required for the design of wind catchers that adapt to the wind direction.
- Using the validated CFD model, we visualized the flow field in the presence of a wind catcher, and demonstrated that a counter-clockwise vortex larger than the size of the canyon is formed when the wind catcher is aligned with the wind direction. This may result in a slight velocity decrease in the immediate downstream canyon; therefore, it is important that the deployment of wind catchers in real environments includes a holistic evaluation including the surrounding canyons.
- We extended the CFD simulations to 3D canyons and found that the characteristics of the canyon vortices are significantly different than in 2D canyons. An improved design of wind catcher with closed sidewalls enhances maximum near-ground wind speed by four times.

The main limitations of the current study and proposed future work are as follows:

- The cases evaluated here are limited in the representation of urban configuration, where only a homogeneous urban area with canyons of aspect ratio 1 is examined. Future work should evaluate the effectiveness of wind catchers in both 2D and 3D canyons with different aspect ratios, and possibly other building arrangements.
- In the present work, only two wind directions with respect to the wind catcher inlet are considered, and the effect of wind direction is not fully included. Accordingly, the results of the reversed wind catcher demonstrate the need for a comprehensive analysis on wind directions that can further inform an effective design of a wind catcher adaptable to the incoming wind direction.
- Future research should incorporate the structural and economical feasibility analyses for the installment of wind catchers in existing urban environments.

Acknowledgments: This research is supported by the National Research Foundation Singapore under its Campus for Research Excellence and Technological Enterprise programme. The Center for Environmental Sensing and Modeling is an interdisciplinary research group of the Singapore-MIT Alliance for Research and Technology. The authors appreciate the discussions with Prof. Rajasekhar Balasubramanian and Dr. Kian Yew Lim on the experimental setup and results analyses. Help from the technical staff in the Hydraulic Engineering Laboratory is acknowledged.

Author Contributions: Lup Wai Chew and Leslie Norford conceived and designed the experiments. Lup Wai Chew conducted the experiments and simulations. Lup Wai Chew and Negin Nazarian analyzed the data and wrote the paper.

Conflicts of Interest: The authors declare no conflict of interest.

Appendix A

CFD model validation should be evaluated in a quantitative way [53]. We adopted two quantitative performance measures: the fractional bias (FB) and the normalized mean-square error (NMSE) in Hanna and Chang [55]:

$$FB = 2(\overline{C_o} - \overline{C_p}) / (\overline{C_o} + \overline{C_p}), \tag{A1}$$

$$NMSE = \overline{(C_o - C_p)^2} / (\overline{C_o} * \overline{C_p}). \tag{A2}$$

C can be any variable, subscript *o* represents observed (or measured), subscript *p* represents predicted (or simulated), and the over-bar represents average (the spatial average of the line profiles in our cases). We calculated FB and NMSE of the line profiles plotted in Figures 11, 13, 14 and 16. Hanna and Chang [55] suggest $|FB| < 0.67$ and $NMSE < 6$ as acceptable criteria for simulations of urban areas. For the mesh independence study (dashed green line and dotted black line) in Figure 11, Table A1 shows that all velocity components, except w/U_{ref} , are well within the acceptable criteria, confirming that mesh independence is achieved. High values of FB and NMSE for w/U_{ref} are due to very small means of w/U_{ref} , as shown in Figure 11b. Since the means of variables appear in the denominators, small values of means will amplify FB and NMSE (in fact, both FB and NMSE approach infinity in the limit of zero means). For CFD model validation, Tables A2–A4 summarize FB and NMSE comparing simulated results with experimental measurements for the reference case (Figure 11), the case with a wind catcher (Figure 13), and the case with a reversed wind catcher (Figure 14), respectively. All three models satisfied the acceptable criteria, except for w/U_{ref} due to the same reason discussed above. Lastly, small FB and NMSE in Table A5 show that both the velocity magnitude and turbulence kinetic energy were well predicted by the model with 3D canyons (Figure 16).

Table A1. Fractional bias (FB) and normalized mean-square error (NMSE) between the simulations with default mesh and refined mesh for the mesh independence study in Section 4.2.

	u/U_{ref}	w/U_{ref}	u'/U_{ref}	w'/U_{ref}
FB	−0.0069	−1.9170	0.0103	0.0103
NMSE	0.0003	679.4798	0.0030	0.0030

Table A2. FB and NMSE between experiment and simulation for the reference case with canyons of aspect ratio 1 in Section 4.2.

	u/U_{ref}	w/U_{ref}	u'/U_{ref}	w'/U_{ref}
FB	0.0080	−1.3691	−0.3332	−0.0118
NMSE	0.0048	33.4916	0.1712	0.0832

Table A3. FB and NMSE between experiment and simulation for the case with a wind catcher in Section 4.3.

	u/U_{ref}	w/U_{ref}	u'/U_{ref}	w'/U_{ref}
FB	0.0032	−4.6399	0.0001	0.0001
NMSE	0.0002	−12.4428	0.0012	0.0012

Table A4. FB and NMSE between experiment and simulation for the case with a reversed wind catcher in Section 4.3.

	u/U_{ref}	w/U_{ref}	u'/U_{ref}	w'/U_{ref}
FB	−0.0145	0.4035	−0.0392	0.3203
NMSE	0.0082	3.7988	0.1221	0.1599

Table A5. FB and NMSE between experiment and simulation for the case with 3D canyons in Section 4.4.

	Velocity Magnitude	tke
FB	0.0323	0.0642
NMSE	0.0146	0.4109

References

- Roth, M. Review of atmospheric turbulence over cities. *Q. J. R. Meteorol. Soc.* **2000**, *126*, 941–990.
- Ng, E. Policies and technical guidelines for urban planning of high-density cities—air ventilation assessment (AVA) of Hong Kong. *Build. Environ.* **2009**, *44*, 1478–1488.
- Gu, Z.L.; Zhang, Y.W.; Cheng, Y.; Lee, S.C. Effect of uneven building layout on air flow and pollutant dispersion in non-uniform street canyons. *Build. Environ.* **2011**, *46*, 2657–2665.
- Zaki, S.A.; Hagishima, A.; Tanimoto, J.; Ikegaya, N. Aerodynamic parameters of urban building arrays with random geometries. *Bound. Layer Meteorol.* **2011**, *138*, 99–120.
- Oke, T.R. Street design and urban canopy layer climate. *Energy Build.* **1988**, *11*, 103–113.
- Li, X.X.; Liu, C.H.; Leung, D.Y. Numerical investigation of pollutant transport characteristics inside deep urban street canyons. *Atmos. Environ.* **2009**, *43*, 2410–2418.
- Hang, J.; Li, Y.; Sandberg, M.; Buccolieri, R.; Di Sabatino, S. The influence of building height variability on pollutant dispersion and pedestrian ventilation in idealized high-rise urban areas. *Build. Environ.* **2012**, *56*, 346–360.
- Oke, T.R. The energetic basis of the urban heat island. *Q. J. R. Meteorol. Soc.* **1982**, *108*, 1–24.
- Oke, T.R. City size and the urban heat island. *Atmos. Environ.* **1973**, *7*, 769–779.
- Arnfield, A.J. Two decades of urban climate research: A review of turbulence, exchanges of energy and water, and the urban heat island. *Int. J. Climatol.* **2003**, *23*, 1–26.
- Rizwan, A.M.; Dennis, L.Y.; Chunho, L. A review on the generation, determination and mitigation of Urban Heat Island. *J. Environ. Sci.* **2008**, *20*, 120–128.
- Santamouris, M.; Cartalis, C.; Synnefa, A.; Kolokotsa, D. On the impact of urban heat island and global warming on the power demand and electricity consumption of buildings—A review. *Energy Build.* **2015**, *98*, 119–124.
- Bueno, B.; Roth, M.; Norford, L.; Li, R. Computationally efficient prediction of canopy level urban air temperature at the neighbourhood scale. *Urban Clim.* **2014**, *9*, 35–53.
- Nazarian, N.; Fan, J.; Sin, T.; Norford, L.; Kleissl, J. Predicting outdoor thermal comfort in urban environments: A 3D numerical model for standard effective temperature. *Urban Clim.* **2017**, *20*, 251–267.
- Santamouris, M.; Papanikolaou, N.; Livada, I.; Koronakis, I.; Georgakis, C.; Argiriou, A.; Assimakopoulos, D. On the impact of urban climate on the energy consumption of buildings. *Sol. Energy* **2001**, *70*, 201–216.
- Hui, S.C. Low energy building design in high density urban cities. *Renew. Energy* **2001**, *24*, 627–640.
- Neophytou, M.K.; Britter, R.E. Modelling the wind flow in complex urban topographies: A Computational-Fluid-Dynamics simulation of the central London area. In Proceedings of the Fifth GRACM International Congress on Computational Mechanics, Limassol, Cyprus, 29 June–1 July 2005; Volume 29.
- Buccolieri, R.; Sandberg, M.; Di Sabatino, S. City breathability and its link to pollutant concentration distribution within urban-like geometries. *Atmos. Environ.* **2010**, *44*, 1894–1903.
- Hang, J.; Li, Y.; Buccolieri, R.; Sandberg, M.; Di Sabatino, S. On the contribution of mean flow and turbulence to city breathability: The case of long streets with tall buildings. *Sci. Total Environ.* **2012**, *416*, 362–373.

20. Panagiotou, I.; Neophytou, M.K.A.; Hamlyn, D.; Britter, R.E. City breathability as quantified by the exchange velocity and its spatial variation in real inhomogeneous urban geometries: An example from central London urban area. *Sci. Total Environ.* **2013**, *442*, 466–477.
21. Di Sabatino, S.; Buccolieri, R.; Salizzoni, P. Recent advancements in numerical modelling of flow and dispersion in urban areas: A short review. *Int. J. Environ. Pollut.* **2013**, *52*, 172–191.
22. Grimmond, C.; Oke, T.R. Aerodynamic properties of urban areas derived from analysis of surface form. *J. Appl. Meteorol.* **1999**, *38*, 1262–1292.
23. Ng, E.; Yuan, C.; Chen, L.; Ren, C.; Fung, J.C. Improving the wind environment in high-density cities by understanding urban morphology and surface roughness: A study in Hong Kong. *Landsc. Urban Plan.* **2011**, *101*, 59–74.
24. Lin, M.; Hang, J.; Li, Y.; Luo, Z.; Sandberg, M. Quantitative ventilation assessments of idealized urban canopy layers with various urban layouts and the same building packing density. *Build. Environ.* **2014**, *79*, 152–167.
25. Ramponi, R.; Blocken, B.; Laura, B.; Janssen, W.D. CFD simulation of outdoor ventilation of generic urban configurations with different urban densities and equal and unequal street widths. *Build. Environ.* **2015**, *92*, 152–166.
26. Kastner-Klein, P.; Rotach, M.W. Mean flow and turbulence characteristics in an urban roughness sublayer. *Bound. Layer Meteorol.* **2004**, *111*, 55–84.
27. Xie, X.; Huang, Z.; Wang, J.S. Impact of building configuration on air quality in street canyon. *Atmos. Environ.* **2005**, *39*, 4519–4530.
28. Hosseini, S.H.; Ghobadi, P.; Ahmadi, T.; Calautit, J.K. Numerical investigation of roof heating impacts on thermal comfort and air quality in urban canyons. *Appl. Therm. Eng.* **2017**, *123*, 310–326.
29. Huang, Y.; Hu, X.; Zeng, N. Impact of wedge-shaped roofs on airflow and pollutant dispersion inside urban street canyons. *Build. Environ.* **2009**, *44*, 2335–2347.
30. Abohela, I.; Hamza, N.; Dudek, S. Effect of roof shape, wind direction, building height and urban configuration on the energy yield and positioning of roof mounted wind turbines. *Renew. Energy* **2013**, *50*, 1106–1118.
31. Aliabadi, A.A.; Krayenhoff, E.S.; Nazarian, N.; Chew, L.W.; Armstrong, P.R.; Afshari, A.; Norford, L.K. Effects of Roof-Edge Roughness on Air Temperature and Pollutant Concentration in Urban Canyons. *Bound. Layer Meteorol.* **2017**, *164*, 149–179.
32. Sharples, S.; Bensalem, R. Airflow in courtyard and atrium buildings in the urban environment: A wind tunnel study. *Sol. Energy* **2001**, *70*, 237–244.
33. Montazeri, H. Experimental and numerical study on natural ventilation performance of various multi-opening wind catchers. *Build. Environ.* **2011**, *46*, 370–378.
34. Montazeri, H.; Azizian, R. Experimental study on natural ventilation performance of one-sided wind catcher. *Build. Environ.* **2008**, *43*, 2193–2202.
35. Dehghan, A.; Esfeh, M.K.; Manshadi, M.D. Natural ventilation characteristics of one-sided wind catchers: Experimental and analytical evaluation. *Energy Build.* **2013**, *61*, 366–377.
36. Li, X.X.; Leung, D.Y.; Liu, C.H.; Lam, K. Physical modeling of flow field inside urban street canyons. *J. Appl. Meteorol. Clim.* **2008**, *47*, 2058–2067.
37. Snyder, W.H. *Guideline for Fluid Modeling of Atmospheric Diffusion*; Technical Report; Environmental Protection Agency: Research Triangle Park, NC, USA, 1981.
38. Meroney, R.N.; Pavageau, M.; Rafailidis, S.; Schatzmann, M. Study of line source characteristics for 2-D physical modelling of pollutant dispersion in street canyons. *J. Wind Eng. Ind. Aerodyn.* **1996**, *62*, 37–56.
39. Baik, J.J.; Park, R.S.; Chun, H.Y.; Kim, J.J. A laboratory model of urban street-canyon flows. *J. Appl. Meteorol.* **2000**, *39*, 1592–1600.
40. Kastner-Klein, P.; Fedorovich, E.; Rotach, M. A wind tunnel study of organised and turbulent air motions in urban street canyons. *J. Wind Eng. Ind. Aerodyn.* **2001**, *89*, 849–861.
41. Brown, M.J.; Lawson, R.; Decroix, D.S.; Lee, R.L. Mean flow and turbulence measurements around a 2-D array of buildings in a wind tunnel. In Proceedings of the 11th joint AMS/AWMA conference on the applications of air pollution meteorology, Long Beach, CA, USA, 9–14 January 2000.
42. Cui, Z.; Cai, X.; J Baker, C. Large-eddy simulation of turbulent flow in a street canyon. *Q. J. R. Meteorol. Soc.* **2004**, *130*, 1373–1394.

43. Salim, S.M.; Buccolieri, R.; Chan, A.; Di Sabatino, S. Numerical simulation of atmospheric pollutant dispersion in an urban street canyon: Comparison between RANS and LES. *J. Wind Eng. Ind. Aerodyn.* **2011**, *99*, 103–113.
44. Dong, J.; Tan, Z.; Xiao, Y.; Tu, J. Seasonal Changing Effect on Airflow and Pollutant Dispersion Characteristics in Urban Street Canyons. *Atmosphere* **2017**, *8*, 43.
45. Memon, R.A.; Leung, D.Y.; Liu, C.H. Effects of building aspect ratio and wind speed on air temperatures in urban-like street canyons. *Build. Environ.* **2010**, *45*, 176–188.
46. Blocken, B.; Stathopoulos, T.; Van Beeck, J. Pedestrian-level wind conditions around buildings: Review of wind-tunnel and CFD techniques and their accuracy for wind comfort assessment. *Build. Environ.* **2016**, *100*, 50–81.
47. ANSYS. Available online: <http://www.ansys.com> (accessed on 16 June 2017).
48. Santiago, J.L.; Martilli, A.; Martín, F. CFD simulation of airflow over a regular array of cubes. Part I: Three-dimensional simulation of the flow and validation with wind-tunnel measurements. *Bound. Layer Meteorol.* **2007**, *122*, 609–634.
49. Li, X.X.; Liu, C.H.; Leung, D.Y. Large-eddy simulation of flow and pollutant dispersion in high-aspect-ratio urban street canyons with wall model. *Bound. Layer Meteorol.* **2008**, *129*, 249–268.
50. Hang, J.; Li, Y.; Sandberg, M. Experimental and numerical studies of flows through and within high-rise building arrays and their link to ventilation strategy. *J. Wind Eng. Ind. Aerodyn.* **2011**, *99*, 1036–1055.
51. Franke, J.; Hirsch, C.; Jensen, A.; Krüs, H.; Schatzmann, M.; Westbury, P.; Miles, S.; Wisse, J.; Wright, N. Recommendations on the use of CFD in wind engineering. In Proceedings of the International Conference on Urban Wind Engineering and Building Aerodynamics, COST Action C14, von Karman Institute, Sint-Genesius-Rode, Belgium, 5–7 May 2004.
52. OpenFOAM. Available online: <http://www.openfoam.com> (accessed on 16 June 2017).
53. Blocken, B. Computational Fluid Dynamics for urban physics: Importance, scales, possibilities, limitations and ten tips and tricks towards accurate and reliable simulations. *Build. Environ.* **2015**, *91*, 219–245.
54. ParaView. Available online: <https://www.paraview.org> (accessed on 16 June 2017).
55. Hanna, S.; Chang, J. Acceptance criteria for urban dispersion model evaluation. *Meteorol. Atmos. Phys.* **2012**, *116*, 133–146.



© 2017 by the authors. Licensee MDPI, Basel, Switzerland. This article is an open access article distributed under the terms and conditions of the Creative Commons Attribution (CC BY) license (<http://creativecommons.org/licenses/by/4.0/>).